Proton Migration in Hybrid Lead Iodide Perovskites: From Classical Hopping to Deep Quantum Tunneling

Yexin Feng,[†,‡,⊥] Yicheng Zhao,[†,⊥] Wen-Ke Zhou,[†] Qi Li,[†] Wissam A. Saidi,[§] Qing Zhao,*[,†,∥] and Xin-Zheng Li*[,†,∥]

[†]State Key Laboratory for Mesoscopic Physics and School of Physics, Peking University, Beijing 100871, P. R. China
[‡]School of Physics and Electronics, Hunan University, Changsha 410082, P. R. China
[§]Department of Mechanical Engineering and Materials Science, University of Pittsburgh, Pittsburgh, Pennsylvania 15261, United States
[∥]Collaborative Innovation Center of Quantum Matter, Peking University, Beijing 100871, P. R. China

S *Supporting Information*

ABSTRACT: The organic−inorganic halide perovskites (OIHPs) have shown enormous potential for solar cells, while problems like the current−voltage hysteresis and the long-term instability have seriously hindered their applications. Ion migrations are believed to be relevant. But the atomistic details still remain unclear. Here we study the migrations of ions in $CH_3NH_3PbI_3$ ($MAPbI_3$) at varying temperatures (T's), using combined experimental and first-principle theoretical methods. Classical hopping of the iodide ions is the main migration mechanism at moderate T's. Below ∼270 K, the kinetic constant for ionic migration still shows an Arrhenius dependency, but the much lower activation energy is attributed to the migration of H^+. A gradual classical-to-quantum transition takes place between ∼140 and ∼80 K. Below ∼80 K, the kinetic constant becomes T-independent, suggesting that deep quantum tunneling of H^+ takes over. This study gives direct experimental evidence for the migrations of H^+s in $MAPbI_3$ and confirms their quantum nature.
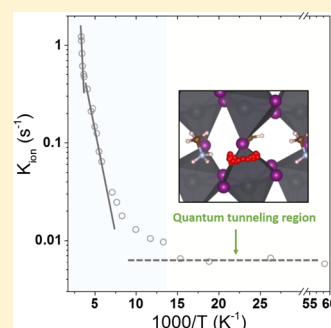
The migration and diffusion of ions are important in chemistry, physics, and material sciences.[1] They are also vital to many technologies relevant to our daily life and future green-energy economy, e.g., batteries, fuel cells, electrocatalysis, and solar cells.[2−4] Among these applications, lithium battery has been commercialized in vehicles and mobiles, and ionic migration is the main charge transport mechanism.[5] In electrocatalysis and fuel cells, the understanding of the ion diffusions in experiment and theory, such as the diffusions of H^+ and metal ions, has played a key role in improving the device performances and facilitating catalyst design.[6] Although fast ionic migration is needed in many applications, it could be detrimental in electronic devices, e.g., electromigration in integrated circuit. For organic−inorganic perovskite solar cells,[7−13] the ionic migration within OIHP active layer has been demonstrated to cause instable power output, the current−voltage ($I−V$) hysteresis and the structural instability, which greatly hindered their applications.[3,4,14−16]

Extensive experimental and theoretical works have been carried out to understand which ion migrates in OIHPs.[17−24] Many kinds of ions, such as Pb^{2+}, MA^+, I^-, and H^+ have been examined. By using photothermal induced resonance (PTIR) microscopy technique, Yuan et al. observed the redistribution and migration of MA^+ after an application of a small electrical field in a $MAPbI_3$ solar cell.[20] Theoretical calculations based on the density-functional theory (DFT) method have suggested that I^- may have lower activation energy than MA^+.[21,22] Few

studies have reported the formation of PbI_2 near the Pb-anode/$MAPbI_3$ interface after an application of a direct-current bias, implying that I^- ions migrate toward the Pb-anode.[23] But this decomposition process may also originate from the reverse flow of MA^+. For H^+ diffusion, Egger et al. reported an activation energy as low as 0.29 eV in $MAPbI_3$,[24] while there is yet no direct experimental evidence to verify the continuous diffusion of H^+, i.e., migration through the whole crystal/polycrystal, in bulk OIHPs. Chen et al. have recently demonstrated a shuttling of H^+ in $MAPbI_3$, which may come from H^+ tunneling between two adjacent iodide ions.[25] But this is a local movement between two sites and it locates in the interfacial region. More recently, Cardenas-Daw et al. suggested that an intrinsic doping of $MAPbI_3$ would most likely be attributed to the transfer of H^+.[26] In spite of these experimental and theoretical, the microscopic details of ionic migration within OIHPs, especially the role of H^+, still remains unclear.

In this Letter, we report a combined experimental and theoretical study of ion diffusions in OIHPs, trying to unravel the dominating ionic migration mechanism at varying T's. We choose $MAPbI_3$ as a prototype material. Since the ion redistribution is a slow process with a time scale of few
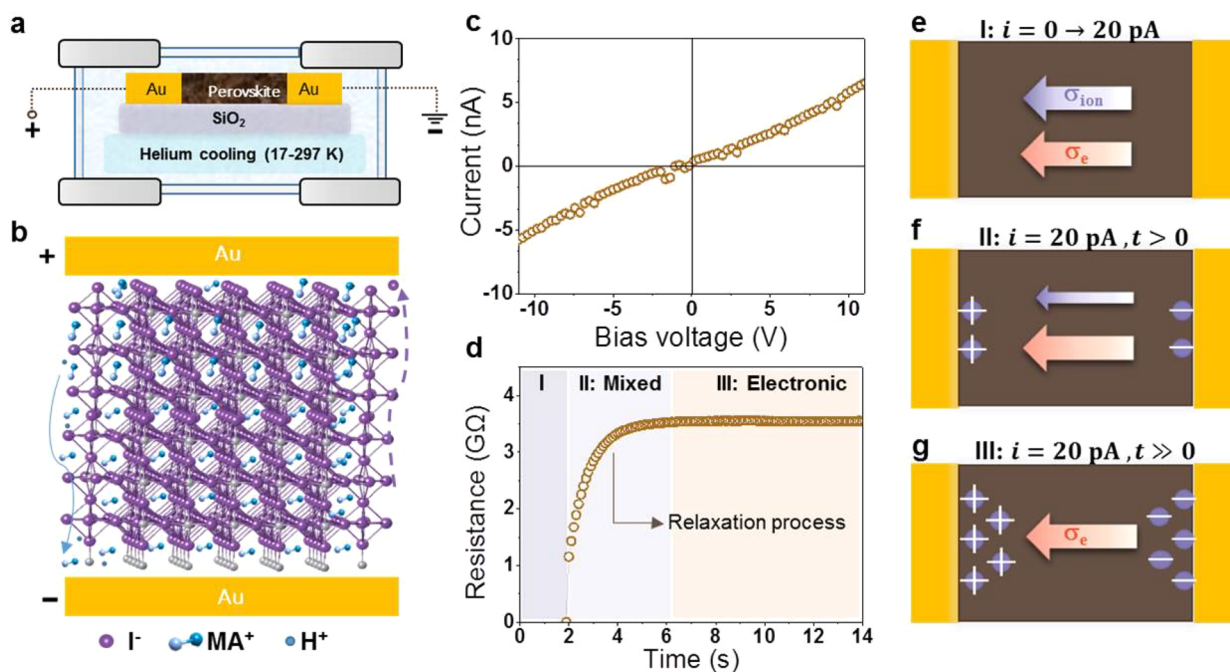
Figure 1. Experimental setup and characterization method for the ionic conductance. (a) Schematic of the measurement setup with a vacuum system, including a cryogenic stage and electrode wires. (b) Illustration of possible ion diffusions in perovskite crystal. (c) Current−voltage measurement with 50 V/s scanning rate on MAPbI$_3$ perovskite film. (d) Galvanostatic characterization on MAPbI$_3$ perovskite film. At 2 s, a constant 20 pA current switches on and the resistance gradually reaches to an equilibrium value due to depleted ion diffusion. (e)−(g) Schematics for conductance contribution in MAPbI$_3$ perovskite film from both ionic transport and electronic transport at different stages during galvanostatic measurement.

seconds, the dynamics of ionic transport can be characterized by the relaxation time in galvanostatic measurement.[18,27−32] In theory, a combination of transition state searching (TSS), *ab initio* molecular dynamics (MD), and *ab initio* path-integral molecular dynamics (PIMD) methods were used. The TSS method treats nuclei as static classical particles.[33,34] *Ab initio* MD includes finite-*T* classical statistical effects, with electronic structures calculated on-the-fly.[35,36] With *ab initio* PIMD, the nuclear quantum effects (NQEs), which are often important in systems involving hydrogen, were further added in on the same footing as the classical statistical effects.[37−42] As such, comparisons between the TSS, the *ab initio* MD, and the *ab initio* PIMD results allow the classical statistical and the NQEs to be addressed in a very clean manner.[36,43−45] The kinetic constant due to ionic migration (K_{ion}) is derived from the relaxation time via galvanostatic characterization between 17 and 297 K. On the basis of the comparison between the experimental observation and theoretical simulations, we find that above ∼270 K, the classical hopping of I$^-$ ion is dominant with an activation energy of ∼0.4 eV. Below ∼270 K, the linear dependency of ln K_{ion} on $1/T$ is retained, but with a much smaller migration activation energy of ∼0.1 eV. Static nuclei simulations for H$^+$ diffusions give barriers ranging from 0.07 to 0.3 eV. NQEs can effectively reduce the H$^+$ diffusion barriers by ∼30−40%. Therefore, classical hopping of H$^+$ is the most likely mechanism in this *T* region. A gradual transition from the classical hopping to the quantum tunneling takes place between ∼140 and ∼80 K. Below ∼80 K, K_{ion} becomes *T*-independent and deep quantum tunneling of H$^+$ is dominant. This study observed the H$^+$ migration changes gradually from being dominated by classical hopping, through shallow quantum tunneling, to deep quantum tunneling as *T* decreases,

which can shed light on understanding of ionic migrations and the quantum nature of H$^+$ transfer in OIHPs.

The *I*−*V* and the galvanostatic characteristics were obtained using an Agilent B2900 series precision source/measure unit. The time duration for the galvanostatic measurement is 0.1 s, and the switched currents for MAPbI$_3$ and CsPbI$_2$Br are 0.02 and 0.01 nA, respectively. After these data were collected, we extract the ionic and electronic conductance. Finally, the ideal formula below was used to obtain conductivity through $\sigma = \frac{GL}{s} \times 10^9 \approx 0.52 \times 10^9 G$ (μs/cm), where G is the conductance, s is the cross-section area, and L is the gap of lateral device. For cryogenic electrical experiments, we use a small-size silica template to prepare Au electrode confined by the sample stage in the chamber, which leaves a 50 μm gap on perovskite film with 50 μm width. The cryogenic experiment was conducted in a cryostation (MONATA C2MODEL) from 17 K to room temperature. The lateral device was directly mounted on the He-cooled cryostat with a temperature controller, in a high-vacuum box with 0.9 μTorr. Measurements were made with temperature increases from 17 to 297 K and stabilized for over 10 min at each temperature. In galvanostatic measurements, three kinds of possible effects may affect our experimental results: geometric-capacitance current, reaction-related pseudocapacitance, and mobile-ion-induced current. We have carefully excluded the influences of these factors, which is discussed in the Supporting Information.

Our DFT simulations were performed using the Vienna ab initio Simulation Package (VASP), with an in house implementation of the *ab initio* constrained MD and constrained centroid PIMD methods.[36,46] The optB88-vdW functional within vdW-DF was used for a better description of the dispersion interactions,[47,48] which are important for
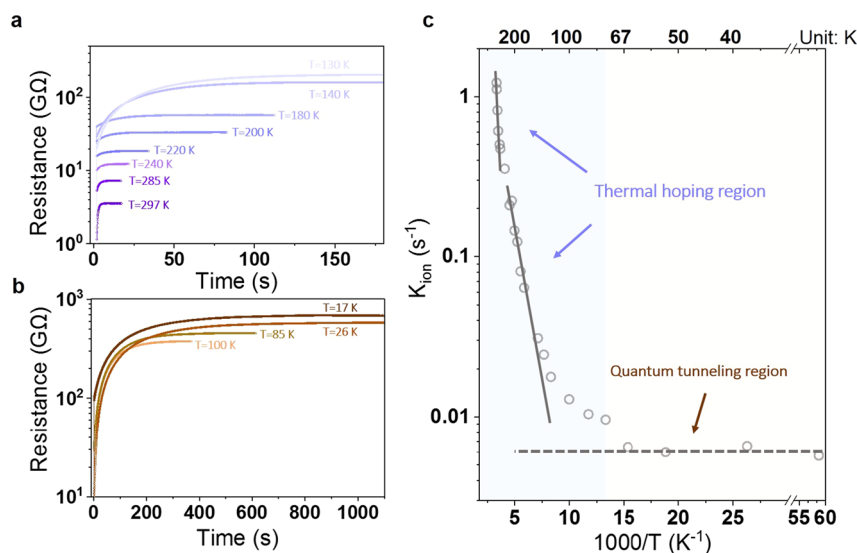
Figure 2. Experimental measurement of the ionic conductance at varying T's. Galvanostatic curves at (a) high (130−297 K) and (b) low temperatures (17−100 K) for the MAPbI$_3$ sample, from which the ionic kinetic constant is derived from exponential fitting for these curves. (c) The ionic kinetic constants vs T for the MAPbI$_3$ perovskite sample.

OIHPs.[49,50] The planewave kinetic-energy cutoff was set to 500 eV. We performed the climbing nudged elastic band (cNEB) method to obtain the static energy profiles for diffusions of ions.[34] Beyond the static description, the classical and quantum free-energy profiles at finite T's were calculated with constrained *ab initio* MD and constrained centroid *ab initio* PIMD methods.[36] More details about these computational setups are provided in the Supporting Information.

A lateral structure Au/MAPbI$_3$/Au on silica substrate was fabricated to perform galvanostatic characterization with sufficiently weak current between 17 and 297 K (Figure 1a). When a bias voltage is applied to the sample, mobile ions (MA$^+$/I$^-$/H$^+$) drift toward the electrodes (Figure 1b). Ionic transport properties, i.e., the kinetic constant K_{ion}, can thus be obtained in galvanostatic measurement. The current−voltage curve of our lateral device shows a linear relationship, indicating a uniform electric field across the device when a bias voltage is applied. This is a standard method in mixed conductor investigations.[28,31,51,52] From previous time-resolved optical spectroscopy study on MAPbI$_3$, we can justify that the time scale of charge and discharge process in MAPbI$_3$ is at least 3 orders of magnitude smaller than ionic accumulation.[53] Therefore, the slow process with the time scale of a few seconds observed in our sample can be safely attributed to the ion migration. We use a two-terminal electrode to test the $I−V$ characteristic of our sample, which shows an ideal linear relationship between I and V. This linear relation indicates the ohmic contact between MAPbI$_3$ and Au. When the current is switched on from zero to a finite value (20 pA for MAPbI$_3$), the measured resistance concomitantly reaches an initial value and then gradually increases to a stable value (Figure 1d). The ionic migration inside the sample is the rate-determining process, while the equilibrium value is determined only by the electronic conductivity σ_e considering the ion-blocking character of Au. Figures 1e−g show a schematic of this evolution. Both electrons and the ions contribute to the conductance when the current is switched on (Figure 1e). We label this region as Region I in Figure 1d. Then, the mobile ions are gradually depleted due to ionic accumulation near the electrodes (schematically shown in Figure 1f, labeled as Region

II in Figure 1d). Finally, the conductance keeps constant with all mobile ions blocked and only electronic conductance remains (schematically shown in Figure 1g), labeled as Region III in Figure 1d. The K_{ion} is extracted by exponential fitting of the relaxation process in Figure 1d and Supplementary Figure S1. We note that the ionic conductivity σ_{ion} can be separated from the total conductivity σ_{total} by subtracting the electronic conductance σ_e using $\sigma_{ion} = \sigma_{total} - \sigma_e$, where the total conductivity is based on the $V−I$ curve in Figure 1c.

The original data for galvanostatic measurements at varying T's is shown in Figure 2a,b. In Figure 2c, we show K_{ion} as a function of $1000/T$. The logarithmic coordinate is chosen for the y axis. Above ∼270 K, $\ln K_{ion}$ depends linearly on $1000/T$. According to the transition state theory (TST), this is a clear indication that the classical hopping of one kind of ions is the dominant mechanism for ion diffusions. The slope indicates an overall activation energy of ∼0.4 eV for the migration of this kind of ion across the bulk, as summarized in Table 1. Below

Table 1. Summary of the Ionic Transporting Behaviors at Different T's Based on the Experimentally Measured K_{ion} and σ_{ion}

K_{ion}		σ_{ion}	
temp range (K)	activation energy (eV) or $\ln K_{ion}$ vs T	temp range	activation energy (eV) or $\ln \sigma_{ion}$ vs T
$T > 285$	∼0.4	$T > 270$	∼0.6
$285 > T > 140$	∼0.1	$270 > T > 140$	∼0.1
$140 > T > 75$	linear slope to horizontal	$140 > T > 8K$	linear slope to horizontal
$75 > T$	horizontal	$85 > T$	horizontal

∼270 K, the linear dependency keeps, but the slope gives a much smaller migration barrier of ∼0.1 eV. In the T range of ∼140 to ∼80 K, we see a gradual transition from linear dependency with a finite slope to a horizontal line. Below ∼80 K, $\ln K_{ion}$ becomes T-independent. Measurements on the conductivity of MAPbI$_3$ show similar results, which are summarized in Supplementary Figure S1 and Table 1. The
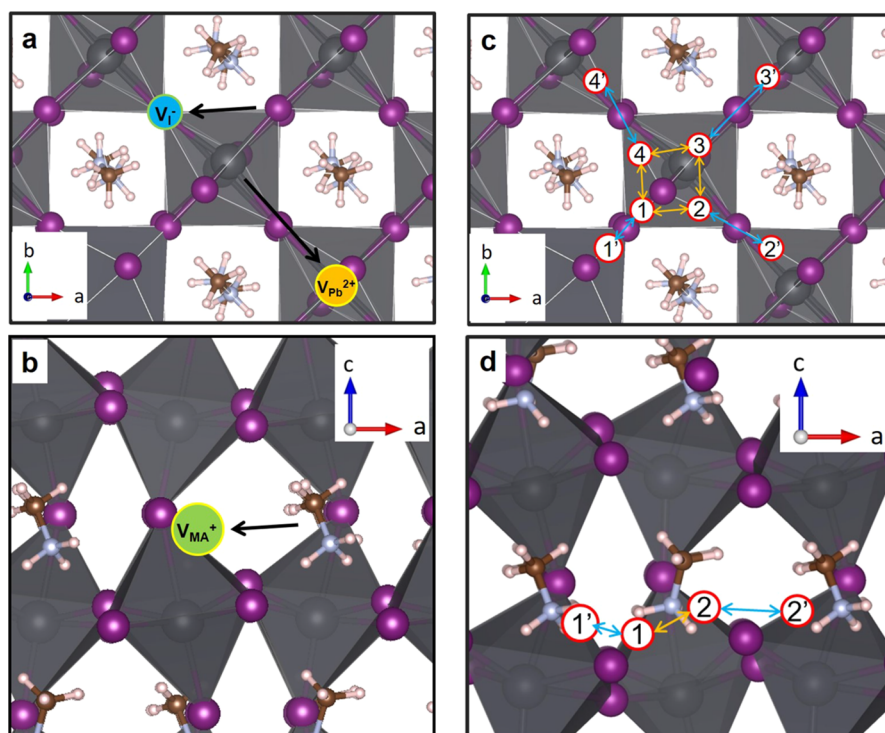
Figure 3. Schematic illustration of different kinds of ionic migration processes in tetragonal phase of MAPbI$_3$. (a) V_I^- hopping along the PbI$_6$ octahedron edge and $V_{Pb^{2+}}$ hopping between neighboring octahedron. (b) V_{MA^-} migration into the neighboring A-site cage. (c) Various proton migration processes within one PbI$_6$ octahedron (1−2, 2−3, 3−4, 4−1) and between neighboring PbI$_6$ octahedrons (1−1′, 2−2′, 3−3′, 4−4′) with a view along the c axis. The red-line circles with numbers inside represent different kinds of sites for proton. (d) Proton migration processes as in (c) but with a view along the b axis. The Black (purple, grown, silver, and pink) balls represent Pb (I, C, N, and H) atoms.

behaviors of ionic migrations as described above still remain, except for a larger activation energy above 270 K and very small differences on the transition T's due to uncertainty of the fitting. The T-independent behavior of ln K_{ion} below 80 K should be related to the deep quantum tunneling of the ions rather than the conventional classical hopping.[36,42] Due to the light mass of H, H$^+$ is the most likely source with which this tunneling can happen. In MAPbI$_3$, H$^+$'s are most likely formed upon deprotonation of MA$^+$.[24,26] To confirm this conjecture, we manufactured the same lateral structure, i.e., Au/CsPbI$_2$Br/Au, using an inorganic material without H (CsPbI$_2$Br). Analysis on the galvanostatic measurement allows the same examination on the relations between kinetic constant ln K_{ion} and $1/T$. In contrast to MAPbI$_3$, we do not observe a constant ln K_{ion} below 80 K, but a constantly increasing tendency until the lowest T we can measure (see Supplementary Figure S2). Therefore, we can safely draw the conclusion that the horizontal lines below ~80 K in Figure 2 are intrinsic to MAPbI$_3$, closely related to the presence of H$^+$.

These experiments provide valuable information for ionic migrations in MAPbI$_3$. To further understand the underlying mechanism, *ab initio* simulations are needed. We do this by using classical static nuclei and resorting to the cNEB method at first. The tetragonal phase of MAPbI$_3$ is chosen to study the ionic diffusion processes within the perovskite lattice.[24] Diffusion channels for vacancy Pb^{2+} ($V_{Pb^{2+}}$), vacancy I$^-$ (V_{I^-}), vacancy MA$^+$ (V_{MA^+}), and interstitial H$^+$ were shown in Figure 3. The cNEB barriers are summarized in Table 2. The experimental diffusion barrier of ~0.4 eV above ~270 K is close to the calculated diffusion barrier of V_{I^-}, whose cNEB barrier is 0.47 eV. The barriers for $V_{Pb^{2+}}$ and V_{MA^+} are much larger, and those for H$^+$ are much smaller. Therefore, the V_{I^-}

Table 2. Theoretical Ionic Diffusion Barriers in MAPbI$_3$[a]

	$V_{Pb^{2+}}$ (eV)	V_{MA^+} (eV)	V_{I^-} (eV)	V_{H^+} (elementary process) (eV)
/ NEB	1.73	0.79	0.47	0.07 (2−3)
				0.30 (4−4′)
ΔF^C				0.27 (1−2)
				0.30 (4−4′)
ΔF^Q				0.17 (1−2)
				0.20 (4−4′)

[a]ΔF^C is obtained from the *ab initio* constrained MD simulations, and ΔF^Q is obtained from the *ab initio* constrained PIMD simulations within the T range 300−75 K. Their differences show the reduction of the activation free-energy due to NQEs.

ions are most likely to be the main diffusive ion above 270 K. Below 270 K, an experimental barrier of ~0.1 eV exists. The various elementary processes for H$^+$ diffusion, as shown in Figure 3c,d, exhibit different barriers, lying between 0.07 and 0.3 eV. The H$^+$ diffusions in the orthorhombic phase of MAPbI$_3$ have also been studied with the cNEB method, which show very small differences with those in the tetragonal phase, as shown in Supplementary Figure S7. At finite T's, fluctuations of the PbI$_6$ octahedron cages allow these H$^+$ transfer channels to interchange. Therefore, from a statistical perspective, the effective H$^+$ transfer energy barrier is likely to take smaller values among them. Additionally, our later theoretical simulations will show that the NQEs can further reduce the classical free-energy barriers by ~30−40%, so H$^+$ should be the only possible source for the σ_{ion} in this T range (270−140 K). Further, the linear dependency of ln K_{ion} on $1/T$ suggests that deep quantum tunneling is weak.[42] Classical
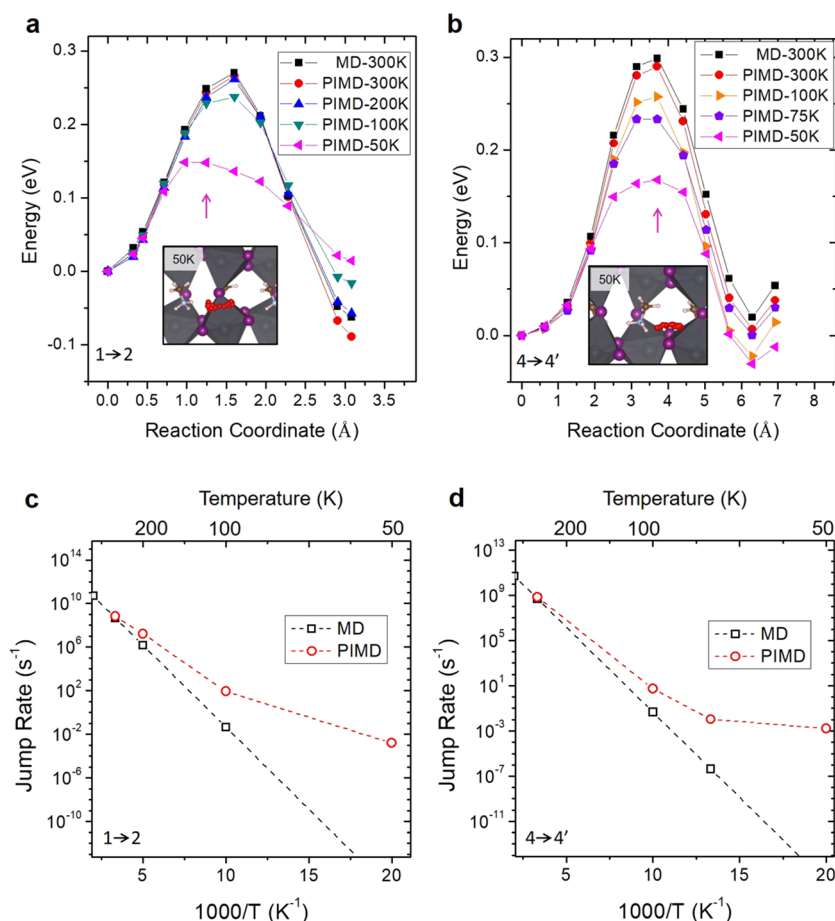
Figure 4. Calculated free-energy profiles and H⁺ jump rates at varying *T*'s. Free-energy profiles obtained with *ab initio* constrained MD and PIMD simulations at varying *T*'s for two rate-limiting proton migration processes, (a) 1−2 and (b) 4−4′. PIMD simulation snapshots for the TS are given as the insets to show the deep tunneling behavior of H⁺. The calculated *T*-dependency of H⁺ jump rates for diffusion processes (c) 1−2 and (d) 4−4′, respectively. Red and black dashed lines represent the calculated quantum and classical hopping rates.

hopping and shallow tunneling are still the dominant mechanisms. Between about 140 and 80 K, we see a typical gradual transition from classical hopping dominating region to quantum tunneling dominating region. Below ∼80 K, the *T*-independent diffusion rate indicates that deep quantum tunneling is the main ionic transport channel. Again, H⁺ is the only possible charged carrier responsible for the deep tunneling behavior.

To quantitatively characterize the quantum tunneling effects, we resort to the path-integral representation of quantum mechanics for the description of the NQEs.[36,44,45] Among the elementary H⁺ transfer processes shown in Figure 3c, which altogether form continuous in-plane diffusion channels, we have chosen the two paths (1−2 and 4−4′) with the highest static energy barriers. This provides the most conservative estimation of NQEs on the H⁺ diffusion. In realistic systems, considering the rotations of the PbI₆ octahedron cages and the smaller barriers of other elementary processes, the reduction of the effective H⁺ transfer energy barrier due to NQEs should be larger. In our simulations, by constraining the centroid of H⁺ at various values along specific reaction coordinate, we can manipulate the H⁺ to migrate between two sites.[36,46,54] The profiles of the mean constrained forces are shown in Supplementary Figure S4, at varying *T*'s for H⁺ transfer processes of 1−2 and 4−4′. By integrating over the forces, we obtained the free-energy profiles (in Figure 4a,b). Then, on the

basis of the classical TST and a practical version of quantum TST,[36,46] we calculate the classical and quantum jump rates (K_C and K_Q) for H⁺. The results are shown in Figure 4c,d. We note that K_Q in Figure 4 and K_{ion} in Figure 2 have about 5 orders of magnitude differences, which is mainly due to the migration length differences between the H⁺ jump process (several Å) and the migration of H⁺ across the Au/MAPbI₃/Au device (50 μm). Moreover, the polycrystalline character of our sample could also affect the K_{ion}, which implies that the absolute values of the theoretical K_Q and the experimental K_{ion} might not be directly comparable. Rather, their *T*-dependencies should be analyzed. With classical nuclei, the barrier height is *T*-independent. TST gives a linear dependency of ln K_c on $1000/T$ with a finite slope corresponding to the magnitude of the activation energy (Figure 4c,d). With quantum nuclei, the mean constrained force weakens at the transition state (TS) due to the delocalization of H⁺. At 50 K, we see a completely delocalized quantum path of the H⁺ in the insets of Figure 4a,b, which significantly reduces the diffusion barrier for H⁺. The *T*-dependency of K_Q gives good theoretical interpretations of the experimental measurements in Figure 2. Substantially linear dependency of ln K_Q on $1000/T$ with a finite slope above 75 K suggests that the deep quantum tunneling is not the dominant mechanism (in Figure 4c,d). Through linear fitting of ln K_Q versus *T* within the *T* range 300−75 K, it is found that shallow quantum tunneling and

zero-point motion effectively reduce the classical free-energy barrier from 0.27 eV to the quantum barrier of 0.17 eV for the $1-2$ process, and from 0.30 to 0.20 eV for the $4-4'$ process (in Table 2). These theoretical results indicate that the experimental measured small barriers of ∼0.1 eV should have large contributions from NQEs. Below 75 K, delocalized quantum proton along the diffusion path as shown in insets of Figure 4a,b and the significant NQEs on $\ln K_Q$ suggest that deep quantum tunneling is dominant.[42] These results show that the proton migration changes gradually from being dominated by classical hopping, through shallow quantum tunneling, to deep quantum tunneling as T decreases and provide a clear theoretical rationalization of our experimental observations.

In summary, we have performed a combined experimental and theoretical study of the T-dependent ionic migrations in MAPbI$_3$. The transition from the classical hopping to the deep quantum tunneling at low T's and the contrasting behaviors of the ionic migrations between hybrid and inorganic lead iodide perovskites provide the first experimental evidence, to the best of our knowledge, for continuous H$^+$ diffusions in MAPbI$_3$. Given the dearth of understanding about the elementary processes of ionic diffusions in OIHPs, especially under varying T's and with the quantum nature of the nuclei taken into account, this study has a number of implications. One important point is that quantum tunneling of H$^+$, a phenomenon often reported in studies of H-bond dynamics, biological processes, chemical physics surface reactions, etc., can be relevant to the performance of this popular condensed matter in green energy research. When coupled with nonadiabatic electronic dynamics,[55] it also suggests that understanding the optical energies beyond the framework of conventional Born–Oppenheimer approximation, in which the interaction between the quantum nature of the nuclei and the nonadiabatic nature of the electronic dynamics is crucial, can also potentially become a subject of cutting-edge studies.[56] Under cryogenic conditions, our results indicate that the conventional classical descriptions of the nuclei are insufficient. Although many earlier theoretical and experimental studies have captured this feature by theoretically addressing the electron–phonon interactions or experimentally analyzing the isotope effects, a quantum treatment of both the electrons and the nuclei is strongly recommended in these systems involving H. We hope this study can stimulate more experimental and theoretical works in these directions.

ASSOCIATED CONTENT

ⓢ Supporting Information

The Supporting Information is available free of charge on the ACS Publications website at DOI: 10.1021/acs.jpclett.8b02929.

> Experimental methods; computational details of DFT calculations and PIMD simulations; experimental results on the ionic conductivities; kinetic constant for the CsPbI$_2$Br perovskite sample at varying temperatures; detailed cNEB calculation results including atomic structures and energy profiles; calculated mean constraint force profiles; illustration of different kinds of H$^+$ diffusion: XRD profiles; impedance spectra; device schematic and resistance vs time graph (PDF)

AUTHOR INFORMATION

Corresponding Authors
*Q. Zhao. E-mail: zhaoqing@pku.edu.cn.
*X.-Z. Li. E-mail: xzli@pku.edu.cn.

ORCID
Yexin Feng: 0000-0001-5925-8645
Qing Zhao: 0000-0003-3374-6901
Xin-Zheng Li: 0000-0003-0316-4257

Author Contributions
⊥Contributed equally to this work

Notes
The authors declare no competing financial interest.

REFERENCES

(1) Steele, B. C. H.; Heinzel, A. Materials for fuel-cell technologies. *Nature* **2001**, *414*, 345−352.

(2) Kojima, A.; Teshima, K.; Shirai, Y.; Miyasaka, T. Organometal halide perovskites as visible-light sensitizers for photovoltaic cells. *J. Am. Chem. Soc.* **2009**, *131*, 6050−6051.

(3) Dualeh, A.; Moehl, T.; Tétreault, N.; Teuscher, J.; Gao, P.; Nazeeruddin, M. K.; Grätzel, M. Impedance spectroscopic analysis of lead iodide perovskite-sensitized solid-state solar cells. *ACS Nano* **2014**, *8*, 362−373.

(4) Xiao, Z.; Yuan, Y.; Shao, Y.; Wang, Q.; Dong, Q.; Bi, C.; Sharma, P.; Gruverman, A.; Huang, J. S. Giant switchable photovoltaic effect in organometal trihalide perovskite devices. *Nat. Mater.* **2015**, *14*, 193−198.

(5) Goodenough, J. B.; Kim, Y. Challenges for Rechargeable Li Batteries. *Chem. Mater.* **2010**, *22*, 587−603.

(6) Norskov, J. K.; Bligaard, T.; Rossmeisl, J.; Christensen, C. H. Towards the computational design of solid catalysts. *Nat. Chem.* **2009**, *1*, 37−46.

(7) Graetzel, M. The light and shade of perovskite solar cells. *Nat. Mater.* **2014**, *13*, 838−842.

(8) Green, M. A.; Ho-Baillie, A.; Snaith, H. J. The emergence of perovskite solar cells. *Nat. Photonics* **2014**, *8*, 506−514.

(9) Dong, Q. F.; Fang, Y. J.; Shao, Y. C.; Mulligan, P.; Qiu, J.; Cao, L.; Huang, J. S. Electron-hole diffusion lengths larger than 175 μm in solution-grown CH3NH3PbI3 single crystals. *Science* **2015**, *347*, 967−970.

(10) Nie, W. Y.; Tsai, H. H.; Asadpour, R.; Blancon, J. C.; Neukirch, A. J.; Gupta, G.; Crochet, J. J.; Chhowalla, M.; Tretiak, S.; Alam, M. A.; et al. High-efficiency solution-processed perovskite solar cells with millimeter-scale grains. *Science* **2015**, *347*, 522−525.

(11) Saidaminov, M. I.; Adinolfi, V.; Comin, R.; Abdelhady, A. L.; Peng, W.; Dursun, I.; Yuan, M.; Hoogland, S.; Sargent, E. H.; Bakr, O. M. Planar-integrated single-crystalline perovskite photodetectors. *Nat. Commun.* **2015**, *6*, 8724.

(12) Yang, W. S.; Park, B. W.; Jung, E. H.; Jeon, N. J.; Kim, Y. C.; U, L. D.; Seok, S. I. Iodide management in formamidinium-lead-halide-based perovskite layers for efficient solar cells. *Science* **2017**, *356*, 1376.

(13) Zhang, L.; Yang, X.; Jiang, Q.; Wang, P.; Yin, Z.; Zhang, X.; Tan, H.; Yang, Y.; Wei, M.; Sutherland, B. R.; et al. Ultra-bright and

highly efficient inorganic based perovskite light-emitting diodes. *Nat. Commun.* **2017**, *8*, 15640.

(14) Yin, W. J.; Yang, J. H.; Kang, J.; Yan, Y.; Wei, S. H. Halide perovskite materials for solar cells: a theoretical review. *J. Mater. Chem. A* **2015**, *3*, 8926−8942.

(15) He, Y.; Wang, S.-Q.; Xue, X.-X.; Zhang, L.; Chen, K.; Zhou, W.-X.; Feng, Y. *Ab initio* study of the moisture stability of lead iodine perovskites. *J. Phys.: Condens. Matter* **2018**, *30*, 355501.

(16) Egger, D. A.; Bera, A.; Cahen, D.; Hodes, G.; Kirchartz, T.; Kronik, L.; Lovrincic, R.; Rappe, A. M.; Reichman, D. R.; Yaffe, O. What Remains Unexplained about the Properties of Halide Perovskites? *Adv. Mater.* **2018**, *30*, 1800691.

(17) Yuan, Y.; Huang, J. Ion Migration in Organometal Trihalide Perovskite and Its Impact on Photovoltaic Efficiency and Stability. *Acc. Chem. Res.* **2016**, *49*, 286−293.

(18) Walsh, A. Principles of chemical bonding and band gap engineering in hybrid organicCinorganic halide perovskites. *J. Phys. Chem. C* **2015**, *119*, 5755−5760.

(19) Egger, D. A.; Edri, E.; Cahen, D.; Hodes, G. Perovskite solar cells: do we know what we do not know? *J. Phys. Chem. Lett.* **2015**, *6*, 279−282.

(20) Yuan, Y.; Chae, J.; Shao, Y.; Wang, Q.; Xiao, Z.; Centrone, A.; Huang, J. Photovoltaic Swithing Mechanism in Lateral Structure Hybrid Perovskite Solar Cells. *Adv. Energy Mater.* **2015**, *5*, 1500615.

(21) Eames, C.; Frost, J. M.; Barnes, P. R. F.; O'Regan, B. C.; Walsh, A.; Islam, M. S. Ionic transport in hybrid lead iodide perovskite solar cells. *Nat. Commun.* **2015**, *6*, 7497.

(22) Haruyama, J.; Sodeyama, K.; Han, L.; Tateyama, Y. First-Principles study of ion diffusion in perovskite solar cell sensitizers. *J. Am. Chem. Soc.* **2015**, *137*, 10048−10051.

(23) Yang, T. Y.; Gregori, G.; Pellet, N.; Grätzel, M.; Maier, J. The Significance of Ion Conduction in a Hybrid Organic-Inorganic Lead-Iodide-Based Perovskite Photosensitizer. *Angew. Chem., Int. Ed.* **2015**, *54*, 7905−7910.

(24) Egger, D. A.; Kronik, L.; Rappe, A. M. Theory of hydrogen migration in organicCinorganic halide perovskites. *Angew. Chem., Int. Ed.* **2015**, *54*, 12437.

(25) Chen, Y. F.; Tsai, Y. T.; Hirsch, L.; Bassani, D. M. Kinetic Isotope Effects Provide Experimental Evidence for Proton Tunneling in Methylammonium Lead Triiodide Perovskites. *J. Am. Chem. Soc.* **2017**, *139*, 16359.

(26) Cardenas-Daw, C.; Simon, T.; Stolarczyk, J. K.; Feldmann, J. Migration of constituent protons in hybrid organic-inorganic perovskite triggers intrinsic doping. *J. Am. Chem. Soc.* **2017**, *139*, 16462−16465.

(27) Yokota, I. On the electronic conductivity of cuprous sulfide: a diffusion theory. *J. Phys. Soc. Jpn.* **1953**, *8*, 595.

(28) Yokota, I. On the theory of mixed conduction with special reference to the conduction in silver sulfide group semiconductors. *J. Phys. Soc. Jpn.* **1961**, *16*, 2213.

(29) Lunkenheimer, P.; Götzfried, T.; Fichtl, R.; Weber, S.; Rudolf, T.; Loidl, A.; Reller, A.; Ebbinghaus, S. G. Apparent giant dielectric constants, dielectric relaxation, and ac-conductivity of hexagonal perovskites $La_{1.2}Sr_{2.7}BO_{7.33}$ (B = Ru, Ir). *J. Solid State Chem.* **2006**, *179*, 3965.

(30) Zhao, Y. C.; Wei, J.; Li, H.; Yan, Y.; Zhou, W. K.; Yu, D. P.; Zhao, Q. A polymer scaffold for self-healing perovskite solar cells. *Nat. Commun.* **2016**, *7*, 10228.

(31) Zhao, Y. C.; Zhou, W. K.; Zhou, X.; Liu, K. H.; Yu, D. P.; Zhao, Q. Quantification of light-enhanced ionic transport in lead iodide perovskite thin films and its solar cell applications. *Light: Sci. Appl.* **2017**, *6*, e16243.

(32) Zhou, W. K.; Zhao, Y. C.; Zhou, X.; Fu, R.; Li, Q.; Zhao, Y.; Liu, K. H.; Yu, D. P.; Zhao, Q. Light-Independent Ionic Transport in Inorganic Perovskite and Ultrastable Cs-Based Perovskite Solar Cells. *J. Phys. Chem. Lett.* **2017**, *8*, 4122−4128.

(33) Henkelman, G.; Jonsson, H. A dimer method for finding saddle points on high dimensional potential surfaces using only first derivatives. *J. Chem. Phys.* **1999**, *111*, 7010−7022.

(34) Henkelman, G.; Uberuaga, B. P.; Jónsson, H. A climbing image nudged elastic band method for finding saddle points and minimum energy paths. *J. Chem. Phys.* **2000**, *113*, 9901.

(35) Tuckerman, M.; Laasonen, K.; Sprik, M.; Parrinello, M. *Ab initio* molecular dynamics simulation of the solvation and transport of hydronium and hydroxyl ions in water. *J. Chem. Phys.* **1995**, *103*, 150−161.

(36) Feng, Y. X.; Chen, J.; Fang, W.; Wang, E. G.; Michaelides, A.; Li, X. Z. Hydrogenation Facilitates Proton Transfer through Two-Dimensional Honeycomb Crystals. *J. Phys. Chem. Lett.* **2017**, *8*, 6009−6014.

(37) Marx, D.; Tuckerman, M. E.; Hutter, J.; Parrinello, M. The nature of the hydrated excess proton in water. *Nature* **1999**, *397*, 601−604.

(38) Lauhon, L. J.; Ho, W. Direct Observation of the Quantum Tunneling of Single Hydrogen Atoms with a Scanning Tunneling Microscope. *Phys. Rev. Lett.* **2000**, *85*, 4566−4569.

(39) Masgrau, L.; Roujeinikova, A.; Johannissen, L. O.; Hothi, P.; Basran, J.; Ranaghan, K. E.; Mulholland, A. J.; Sutcliffe, M. J.; Scrutton, N. S.; Leys, D. Atomic description of an enzyme reaction dominated by proton tunneling. *Science* **2006**, *312*, 237−241.

(40) Ceriotti, M.; Cuny, J.; Manolopoulos, D. E. Nuclear quantum effects and hydrogen bond fluctuations in water. *Proc. Natl. Acad. Sci. U. S. A.* **2013**, *110*, 15591.

(41) Rossi, M.; Ceriotti, M.; Manolopoulos, D. E. Nuclear Quantum Effects in H+ and OĤC Diffusion along Confined Water Wires. *J. Phys. Chem. Lett.* **2016**, *7*, 3001−3007.

(42) Fang, W.; Richardson, J. O.; Chen, J.; Li, X.-Z.; Michaelides, A. Simultaneous Deep Tunneling and Classical Hopping for Hydrogen Diffusion on Metals. *Phys. Rev. Lett.* **2017**, *119*, 126001.

(43) Marx, D.; Parrinello, M. Structural quantum effects and three-centre two-electron bonding in CH_5^+. *Nature* **1995**, *375*, 216.

(44) Tuckerman, M. E.; Marx, D.; Klein, M. L.; Parrinello, M. Efficient and general algorithms for path integral CarCParrinello molecular dynamics. *J. Chem. Phys.* **1996**, *104*, 5579.

(45) Feng, Y. X.; Chen, J.; Alfè, D.; Li, X. Z.; Wang, E. G. Nuclear quantum effects on the high pressure melting of dense lithium. *J. Chem. Phys.* **2015**, *142*, 064506.

(46) Feng, Y. X.; Wang, Z. C.; Guo, J.; Chen, J.; Wang, E. G.; Jiang, Y.; Li, X. Z. The collective and quantum nature of proton transfer in the cyclic water tetramer on NaCl(001). *J. Chem. Phys.* **2018**, *148*, 102329.

(47) Klimeš, J.; Bowler, D. R.; Michaelides, A. Chemical accuracy for the van der Waals density functional. *J. Phys.: Condens. Matter* **2010**, *22*, 022201.

(48) Klimeš, J.; Bowler, D. R.; Michaelides, A. Van der Waals density functionals applied to solids. *Phys. Rev. B: Condens. Matter Mater. Phys.* **2011**, *83*, 195133.

(49) Saidi, W. A.; Choi, J. J. Nature of the cubic to tetragonal phase transition in methylammonium lead iodide perovskite. *J. Chem. Phys.* **2016**, *145*, 144702.

(50) Shan, W.; Saidi, W. A. Segregation of Native Defects to the Grain Boundaries in Methylammonium Lead Iodide Perovskite. *J. Phys. Chem. Lett.* **2017**, *8*, 5935−5942.

(51) Yang, T. Y.; Gregori, G.; Pellet, N.; Gratzel, M.; Maier, J. The significance of ion conduction in a hybrid organic-inorganic lead-iodide-based perovskite photosensitizer. *Angew. Chem., Int. Ed.* **2015**, *54*, 7905−7910.

(52) Riess, I. Mixed ionic-electronic conductors-material properties and applications. *Solid State Ionics* **2003**, *157*, 1−17.

(53) Peng, J.; Chen, Y.; K, Z.; Pullerits, T.; Liang, Z. Insights into charge carrier dynamics in organo-metal halide perovskites: from neat films to solar cells. *Chem. Soc. Rev.* **2017**, *46*, 5714.

(54) Drechsel-Grau, D.; Marx, D. Quantum simulation of collective proton tunneling in hexagonal ice crystals. *Phys. Rev. Lett.* **2014**, *112*, 148302.

(55) Long, R.; Fang, W.-H.; Prezhdo, O. V. Strong Interaction at the Perovskite/TiO2 Interface Facilitates Ultrafast Photoinduced Charge

Separation: A Nonadiabatic Molecular Dynamics Study. *J. Phys. Chem. C* **2017**, *121*, 3797−3806.

(56) Chen, Y. F.; Tsai, Y. T.; Hirsch, L.; Bassani, D. M. Kinetic isotope effects provide experimental evidence for proton tunneling in methylammonium lead Triiodide Perovskites. *J. Am. Chem. Soc.* **2017**, *139*, 16359−16364.